AAAS
Research
Volume 2019, Article ID 9282674, 9 pages
https://doi.org/10.34133/2019/9282674

Research Article

Reactive Inorganic Vapor Deposition of Perovskite Oxynitride Films for Solar Energy Conversion

Tao Fang,[1] **Huiting Huang**,[1,2] **Jianyong Feng**,[1,2] **Yingfei Hu**,[1,2] **Qinfeng Qian**,[1,2] **Shicheng Yan**,[1,2,3] **Zhentao Yu**,[1,2,3] **Zhaosheng Li**,[1,2,3] **and Zhigang Zou**[1,2,3]

[1]*Collaborative Innovation Center of Advanced Microstructures, National Laboratory of Solid State Microstructures, Department of Physics, Nanjing University, 22 Hankou Road, Nanjing 210093, China*
[2]*College of Engineering and Applied Sciences, Nanjing University, 22 Hankou Road, Nanjing 210093, China*
[3]*Jiangsu Key Laboratory for Nano Technology, Nanjing University, 22 Hankou Road, Nanjing 210093, China*

Correspondence should be addressed to Zhaosheng Li; zsli@nju.edu.cn

Received 3 July 2019; Accepted 7 October 2019; Published 11 November 2019

Copyright © 2019 Tao Fang et al. Exclusive Licensee Science and Technology Review Publishing House. Distributed under a Creative Commons Attribution License (CC BY 4.0).

The synthesis of perovskite oxynitrides, which are promising photoanode candidates for solar energy conversion, is normally accomplished by high-temperature ammonolysis of oxides and carbonate precursors, thus making the deposition of their planar films onto conductive substrates challenging. Here, we proposed a facile strategy to prepare a series of perovskite oxynitride films. Taking $SrTaO_2N$ as a prototype, we prepared $SrTaO_2N$ films on Ta foils under NH_3 flow by utilizing the vaporized $SrCl_2/SrCO_3$ eutectic salt. The $SrTaO_2N$ films exhibit solar water-splitting photocurrents of 3.0 mA cm^{-2} at 1.23 V vs. RHE (reversible hydrogen electrode), which increases by 270% compared to the highest photocurrent (1.1 mA cm^{-2} at 1.23 V vs. RHE) of $SrTaO_2N$ reported in the literature. This strategy may also be applied to directly prepare a series of perovskite oxynitride films on conductive substrates such as $ATaO_2N$ (A = Ca, Ba) and $ANbO_2N$ (A = Sr, Ba).

1. Introduction

Perovskite oxynitrides, which may have the advantages of both oxides and nitrides [1], emerge as an important class of materials due to their promising applications in pigments [2], dielectrics [3, 4], ferroelectrics [5], colossal magnetoresistance [6], and photocatalysis [7, 8]. They usually have smaller bandgap than those of prototypical oxides and better chemical stability than those of prototypical nitrides. Perovskite oxynitrides are currently predicted to be promising candidates for photoelectrochemical (PEC) water splitting [9], which is a potential way to harness solar energy [10–19].

To date, only some particle-assembled oxynitride films (such as $LaTiO_2N$, $BaTaO_2N$, $SrTaO_2N$, and $LaTaON_2$) have been investigated for PEC water splitting [20–24]. In order to prepare the particle-assembled oxynitride films, the oxynitride powders are firstly synthesized by nitridation of corresponding oxide precursors at high temperature under ammonia flow usually at 800~1300°C [5, 25–29]. Subsequently, the particle-assembled oxynitride films are prepared by electrophoretic deposition or particle transfer methods [20–24]. However, these particle-assembled films often suffer from poor charge carrier transport not only among film particles but also between the film particles and the conductive substrate. Also, the efficiency loss may even occur at the exposed region of the underlying conductive substrate [30, 31]. Various efforts have been made to improve their PEC performances, such as increasing the particle crystallinity or H_2 annealing to prompt the charge transport in film particles, and using necking treatment to ameliorate the charge transport among film particles [20–24]. Unfortunately, the electron-hole recombination at the interface between the film particles and conductive substrate is still serious in these particle-assembled films, thus hampering their solar-to-hydrogen efficiency.

It is indispensable and challenging to directly synthesize oxynitride photoanode films on a conductive substrate for overcoming the main shortcomings of the particle-assembled films, including the poor charge carrier transport and the efficiency loss at the exposed conductive substrate. Here, we have presented a strategy of reactive inorganic vapor deposition and prepared a series of oxynitride films,

for example, $SrTaO_2N$. The as-prepared $SrTaO_2N$ photoanode films exhibit a significant increase in the photocurrent as well as photochemical stability and a cathodic shift in onset potential for water oxidation, in comparison with the particle-assembled photoanode films.

2. Results

In this study, we have prepared $SrTaO_2N$ photoanode films by reactive inorganic vapor deposition, as illustrated in Figure 1(a). $SrCl_2$ (74%)/$SrCO_3$ (26%) eutectic salt is used to generate $SrCl_2$ vapor during the nitridation process and provide an Sr source for the formation of $SrTaO_2N$. The CO_2 released from $SrCO_3$ upon the nitridation process is employed as an oxidant to oxidize Ta to Ta^{5+} [32]. Ta foil is used both as a Ta source and as a conductive substrate. The $SrCl_2/SrCO_3$ eutectic salt may be evaporated during the ammonolysis process at 950°C for 2 hours, which is approximately 280°C higher than their melting temperature, according to the phase diagram in Figure S1 [33]. The vaporized flux and released CO_2 react with the Ta foils under the ammonia atmosphere, resulting in the formation of $SrTaO_2N$ film on Ta foil. The morphology of the $SrTaO_2N$ films was analyzed using field-emission scanning electron microscopy (SEM). The top-down image (Figure S2) and cross-sectional image (Figure 1(b)) show that the $SrTaO_2N$ film is a crack-free film consisting of compact and octahedron-like grains; the close contact between the $SrTaO_2N$ film and Ta substrate is propitious to charge carrier transport.

The X-ray diffraction (XRD) pattern (shown in Figure 2(a)) confirms the synthesis of the $SrTaO_2N$ film, based on the JCPDS file (PDF#40-0662). The high-resolution transmission electron microscopy (HRTEM) image of Figure 2(b) displays a lattice spacing of 0.286 nm, corresponding to the $SrTaO_2N$ (1 1 0) facet. The HRTEM image and selected area electron diffraction (SAED) pattern (Figure S3) suggest that the $SrTaO_2N$ samples exhibit high crystallinity, which favors electron transport.

The cross section of the $SrTaO_2N$ film was further studied by TEM. As shown in Figure 3(a), the formation of a TaN subnitride layer can be observed between the $SrTaO_2N$ film and Ta substrate, which is suggested by selected area electron diffraction (SAED) images (Figures 3(b) and 3(c)). The presence of a highly conductive TaN phase provides an efficient electron transfer pathway that benefits the electron transfer from the $SrTaO_2N$ film to Ta substrate. The electrical conductivity of as-prepared $SrTaO_2N$ film photoanode is estimated to be 1.82×10^{-5} S cm^{-1} (derived from Figure S4), which is approximately 23.6 times of 0.77×10^{-6} S cm^{-1} for the particle-assembled $SrTaO_2N$ photoanode [34]. The $SrTaO_2N$ films prepared by our method exhibit much higher conductivity than the particle-assembled films, which may be ascribed to the reduction in the interfacial resistance.

The combination of TG-DTA (thermogravimetric and differential thermal analysis) and mass spectral measurements for the $SrCO_3/SrCl_2$ eutectic salt sample and $SrCO_3/SrCl_2$ eutectic salt+Ta sample was carried out to study the formation mechanism of $SrTaO_2N$, as shown in Figure 4. The weight loss in the temperature range of approximately 70°C to 170°C is caused by the loss of crystal water in $SrCl_2/SrCO_3$ eutectic salt, which is confirmed by the H_2O signal in mass spectra. $SrCO_3$ started to decompose in the temperature range of approximately 550°C to 800°C, according to the weight loss (Figure 4(a)) and CO_2 signal in mass spectra. Compared with the $SrCl_2/SrCO_3$ eutectic salt sample, the $SrCO_3/SrCl_2$ eutectic salt+Ta sample exhibited a weight increase and a peak of H_2O signal in mass spectra around 750°C, which may be an evidence of nitridation reaction.

Control experiments were also carried out by nitriding Ta foils in the same condition with different components of the flux reagent. In the case of the $SrCl_2$ flux reagent, only small amount of $TaN_{0.04}$ and Ta_2N was obtained, as shown in the XRD pattern of Figure S5a. Without the presence of carbonate, there is no CO_2 released during the nitridation process, metallic Ta cannot be nitrided to high-oxidation-state nitride directly by ammonia upon this condition, which is consistent with literatures [32, 35]. Using only $SrCO_3$ as the flux reagent, Ta_3N_5 instead of $SrTaO_2N$ was obtained (Figure S5b). These results indicate that both the $SrCl_2$ flux vapor and CO_2 released from $SrCO_3$ are crucial for the formation of $SrTaO_2N$.

There are no chlorine impurities left on the $SrTaO_2N$ film, according to XPS spectra (Figure S6). The carbon in the films was analyzed by XPS, as shown in Figure S7. The C1s spectra of the $SrTaO_2N$ film show a peak at 284.6 eV, corresponding to the surface adventitious carbon. And the TEM and HRTEM images (Figure S8) suggested that there is no amorphous carbon on the surface of $SrTaO_2N$ particles. Therefore, the reaction equation for the formation of $SrTaO_2N$ films may be written as follows:

$$4Ta + 4SrCl_2 + 5CO_2 + 4NH_3 \longrightarrow 4SrTaO_2N + 8HCl + 5C + 2H_2O \quad (1)$$

In order to find the optimal composition of the $SrCl_2/SrCO_3$ flux reagent for the synthesis of $SrTaO_2N$ film photoanodes, control experiments were also carried out by nitriding Ta foils in the same condition with different compositions of the $SrCl_2/SrCO_3$ flux reagent (50%/50%, 74%/26%, and 80%/20%). The $SrTaO_2N$ film photoanode prepared with $SrCl_2$ (74%)/$SrCO_3$ (26%) eutectic salt exhibits the best PEC performance, as shown in Figure S9. The photocurrent of $SrTaO_2N$ photoanode prepared with the $SrCl_2$ (50%)/$SrCO_3$ (50%) flux reagent at 1.23 V vs. RHE (2.0 mA cm^{-2}) is only 66.7% of that of $SrTaO_2N$ photoanode prepared with $SrCl_2$ (74%)/$SrCO_3$ (26%) eutectic salt (3.0 mA cm^{-2}). The melting temperatures of the $SrCl_2$ (50%)/$SrCO_3$ (50%) flux reagent, $SrCl_2$ (74%)/$SrCO_3$ (26%) eutectic salt and $SrCl_2$ (80%)/$SrCO_3$ (20%) flux reagent are 870°C, 670°C and 715°C, respectively, according to the phase diagram in Figure S1. When using the $SrCl_2$ (50%)/$SrCO_3$ (50%) flux reagent as a precursor, approximately half of the flux reagent remained in the alumina combustion boat after the 2 hours of the nitridation process. These results suggested that the $SrCl_2$ (74%)/$SrCO_3$ (26%) eutectic salt with the lowest melting

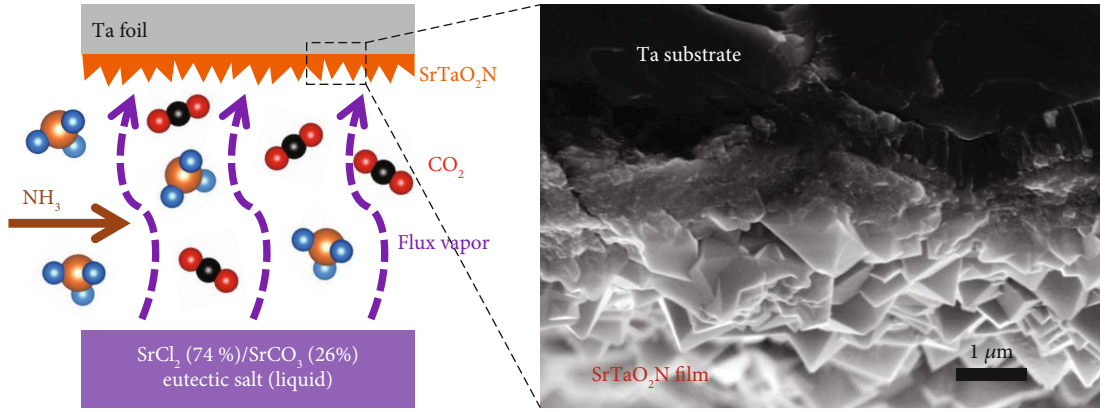

Figure 1: Schematic illustration. (a) Schematic illustration of the reactive inorganic vapor deposition method. (b) Cross-sectional SEM image of the as-prepared $SrTaO_2N$ film.

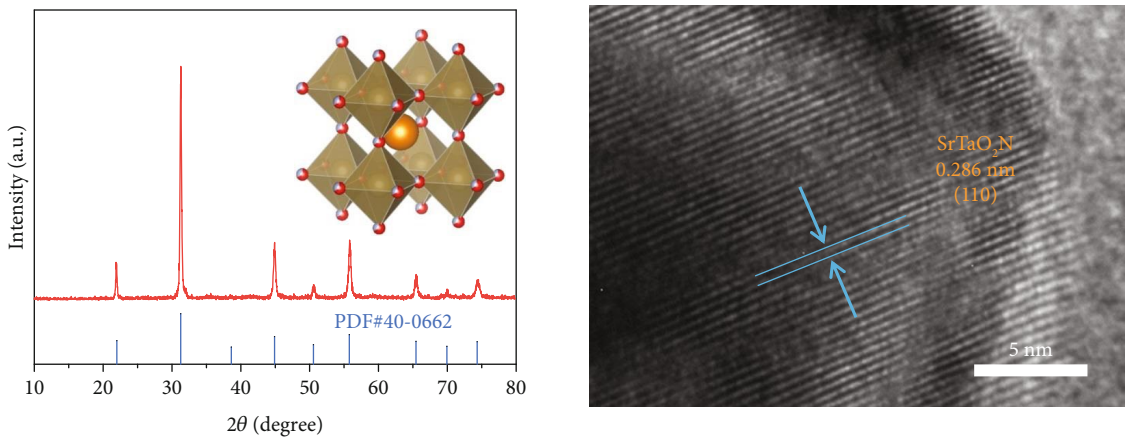

Figure 2: XRD pattern and HRTEM image. XRD pattern (a) and HRTEM image (b) of the as-prepared $SrTaO_2N$ film. The inset shows the crystal structure of $SrTaO_2N$.

temperature may introduce the highest Sr partial pressure during the nitridation process, thus resulting in the best PEC performance of $SrTaO_2N$ film photoanode.

Co/CoOOH catalyst layers were deposited onto the $SrTaO_2N$ photoanode films by a two-step electrodeposition method [36]. A photoassisted electrodeposition method [37] was adopted to produce a conformal CoOOH layer on the $SrTaO_2N$ film by deposition on only where photoinduced holes were generated. The SEM image indicates the conformal distribution of the CoOOH layer on the $SrTaO_2N$ photoanodes (Figure S10a). As illustrated in Figure 5(a), with the surface decoration Co/CoOOH catalyst layers, the $SrTaO_2N$ film photoanode synthesized by the reactive inorganic vapor deposition method (RVD $SrTaO_2N$) exhibits a solar photocurrent of 3.0 mA cm^{-2} at 1.23 V vs. RHE and a low onset potential for water oxidation at 0.55 V vs. RHE. The highest PEC performance of particle-assembled $SrTaO_2N$ photoanodes (particle-assembled $SrTaO_2N$) in the literature exhibits a solar photocurrent of 1.1 mA cm^{-2} at 1.23 V vs. RHE and an onset potential of 0.6 V vs. RHE for water oxidation (Figure 5(a), blue curves) [34]. Compared with the particle-assembled $SrTaO_2N$ photoanode, the directly prepared $SrTaO_2N$ film photoanode shows a ca. 270% enhancement in the photocurrent at 1.23 V vs. RHE and a ca. 50 mV cathodic shift in onset potential for water oxidation. The wavelength dependence of the incident photon-to-current conversion efficiency (IPCE) of the $SrTaO_2N$ film photoanode is shown in Figure 5(b). The onset wavelength for the photocurrents is about 600 nm, which agrees well with the optical absorption edge of $SrTaO_2N$ (Figure S11a). The integrated photocurrent is 2.9 mA cm^{-2} at 1.23 V vs. RHE, which is calculated by multiplication of the measured IPCE spectra with the AM 1.5G standard solar spectral distribution (Figure S12). It agrees well with the experimental photocurrent of 3.0 mA cm^{-2} at 1.23 V vs. RHE in Figure 5(a). The small difference between the integrated and experimental photocurrents suggests that the IPCE spectra and the photocurrent under AM 1.5G illumination are credible.

The applied bias photon-to-current efficiency (ABPE) of the $SrTaO_2N$ films calculated by using the J-V curve (Figure 5(a)) is shown in Figure S13, assuming 100%

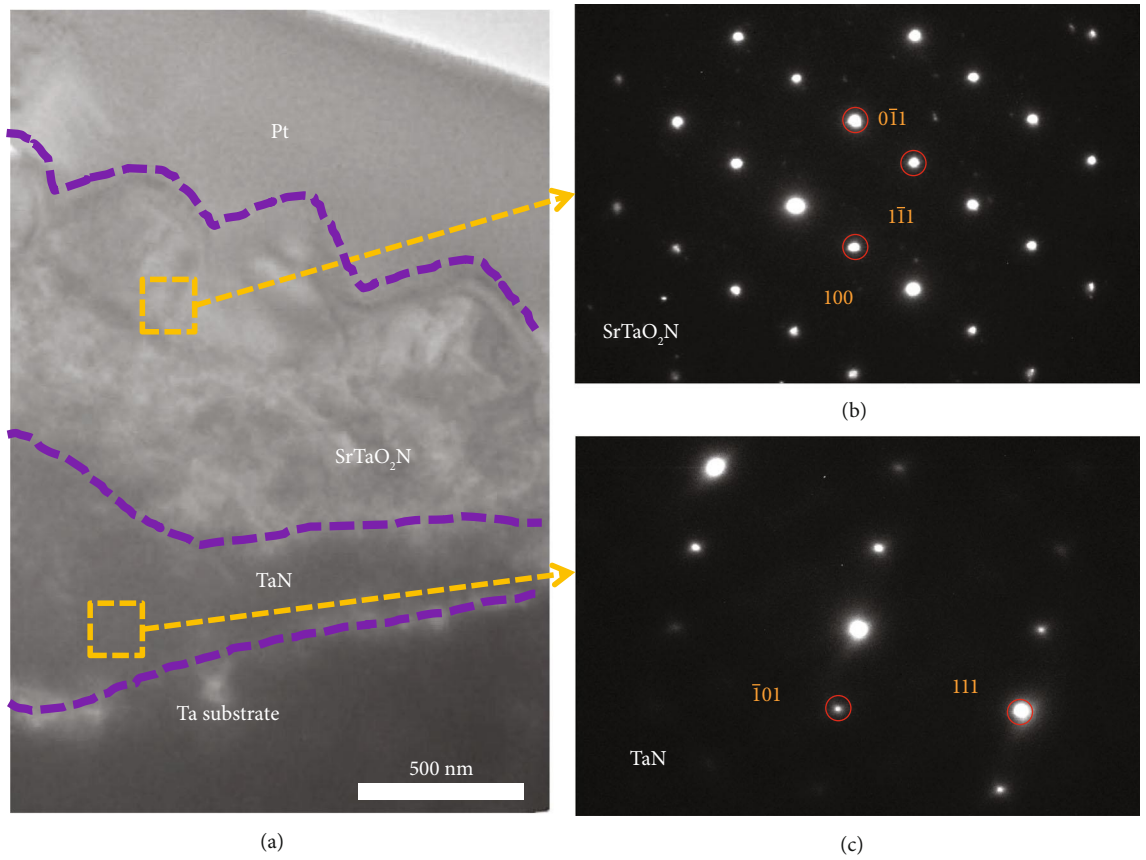

Figure 3: Cross-sectional TEM and SAED images of the $SrTaO_2N$ film. Cross-sectional TEM image (a) and SAED images (b, c) at different depths of the $SrTaO_2N$ film.

faradaic efficiency. The maximum ABPE is 0.53% at 0.85 V vs. RHE for $SrTaO_2N$ film photoanode, which is ca. 3.5 times higher than that of 0.15% at 0.9 V vs. RHE for particle-assembled $SrTaO_2N$ photoanode. Gas chromatography was used to demonstrate that H_2 and O_2 gases evolved during PEC water splitting in a stoichiometric ratio of 2 : 1, and the faradaic efficiency was 93% for H_2 and 94% for O_2, respectively (Figure 5(c)). The band gap and flat band potentials (E_{fb}) of the $SrTaO_2N$ film photoanode were investigated by the Tauc plot (Figure S11b) and Mott-Schottky plots (Figure S14), respectively. These results show that the band gap of $SrTaO_2N$ is approximately 2.1 eV, and the conduction and valence band edges for $SrTaO_2N$ are estimated to be -0.5 and 1.6 V vs. RHE, respectively, which agrees well with previous report [38].

Photochemical stability is a vital parameter for the application of solar water splitting. The $SrTaO_2N$ film photoanode exhibits an initial photocurrent of approximately 2.8 mA cm^{-2} and retains approximately 86% of its initial activity after AM 1.5G (100 mW cm^{-2}) irradiation for 5 hours, which shows significant improvement compared with the particle-assembled $SrTaO_2N$ photoanodes, as shown in Figure 5(d). The improvement in the stability may be ascribed to not only the close contact between $SrTaO_2N$ grains but also the highly conductive TaN phase benefiting the electron transfer from the $SrTaO_2N$ film to Ta substrate. The gradual drop of the photocurrent is partly caused by the peeling off and the dissolution of the CoOOH layer in strong base (1 M NaOH, pH = 13.6) during the stability testing (Figure S10b). Similar phenomenon has also been observed that the CoOOH electrocatalyst shows a steady decrease in the current density for oxygen evolution reaction in 1 M KOH [36].

Electrochemical impedance spectroscopy measurements were performed in a three-electrode configuration with frequencies ranging from 0.1 Hz to 100 kHz, in order to further comprehend the charge transport of these two $SrTaO_2N$ photoanodes. The Nyquist plots of the $SrTaO_2N$ photoanodes (shown in Figure 6) reveal two semicircles. The impedance spectra have been modelled to an equivalent circuit model consisting of two parallel RC elements connected in series, which is shown in the inset of Figure 6(b). The first RC element represents the bulk processes (R_{bulk}, C_{bulk}), and the second represents the surface processes (R_{ct}, C_{sc}). R_s is the electrolyte resistance. The fitted results (Table S1) show that the bulk charge transfer resistance R_{bulk} of the $SrTaO_2N$ film photoanode is only 2% of that of the particle-assembled $SrTaO_2N$ photoanode, thus resulting in a better PEC performance.

The simplicity and rapidity of this process are applicable to a wide range of oxynitride films. For example, $CaTaO_2N$ and $BaTaO_2N$ films were synthesized at the same condition

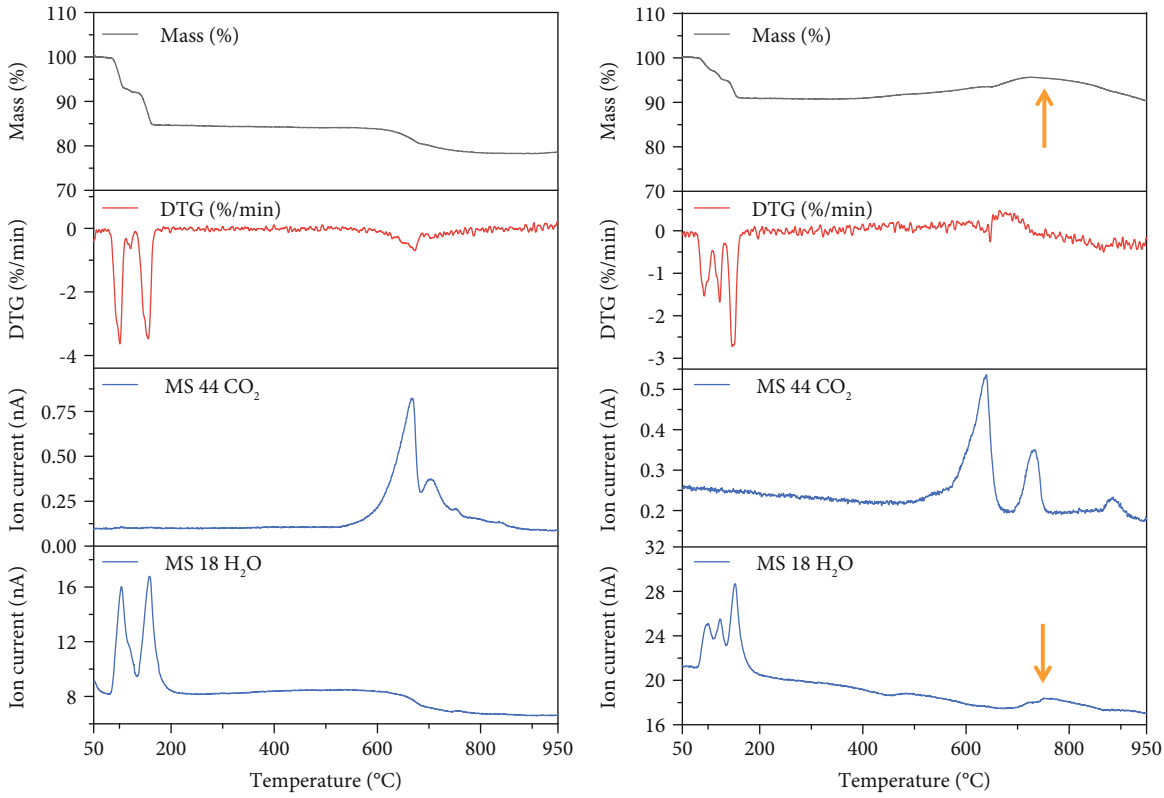

Figure 4: The combination of TG-DTA and mass spectroscopy. Thermogravimetric analysis (TG), differential thermal gravity (DTG), and mass spectra of the $SrCl_2/SrCO_3$ eutectic salt (26 mol% $SrCO_3$, 74 mol% $SrCl_2{\cdot}6H_2O$) (a) and the $SrCO_3/SrCl_2$ eutectic salt+Ta (the mass ratio of the eutectic salt and the Ta powder is 2 : 1) (b).

by using the $CaCl_2/CaCO_3$ flux and $BaCl_2/BaCO_3$ flux, respectively, which are proven by their XRD patterns in Figure S15. As-prepared $CaTaO_2N$ and $BaTaO_2N$ films are similar crack-free and large-grained films (Figure S16). The HRTEM images of $CaTaO_2N$ and $BaTaO_2N$ films display a lattice spacing of 0.280 nm and 0.292 nm (Figure S17), corresponding to $CaTaO_2N$ (2 0 0) and $BaTaO_2N$ (1 1 0), respectively. Moreover, $SrNbO_2N$ and $BaNbO_2N$ films were also synthesized at the same condition by using Nb foil and corresponding flux ($SrCl_2/SrCO_3$ flux for the $SrNbO_2N$ film, $BaCl_2/BaCO_3$ flux for the $BaNbO_2N$ film) as precursors. The XRD patterns confirm the synthesis of $SrNbO_2N$ and $BaNbO_2N$ films; the morphology of $SrNbO_2N$ and $BaNbO_2N$ films exhibit similar large-grained films (Figure S18). The PEC performance of these films was also measured as shown in Figure S19. The PEC performance of these oxynitride films may be further optimized by choosing the optimal composition of the corresponding flux reagent to generate higher Ca or Ba partial pressure during the nitridation process.

3. Discussion

In this study, a series of perovskite oxynitride films such as $ATaO_2N$ (A = Ca, Sr, and Ba) and $ANbO_2N$ (A = Sr, Ba) have been prepared by the reactive inorganic vapor deposition method. As-prepared $SrTaO_2N$ film photoanode exhibits much better PEC performances than the traditional particle-assembled $SrTaO_2N$ photoanode. Solar water-splitting photocurrent of 3.0 mA cm^{-2} at 1.23 V vs. RHE over the $SrTaO_2N$ film photoanode is increased by 270%, compared with the highest photocurrent of the particle-assembled $SrTaO_2N$ photoanode in the literature. Also, the photocurrent remains 86% of its initial activity after AM 1.5G illumination for 5 h, suggesting much better photochemical stability of the $SrTaO_2N$ film photoanode than the particle-assembled $SrTaO_2N$ photoanode. The improvement in the PEC performances may be ascribed to less bulk resistance of the directly prepared $SrTaO_2N$ films. The concept of reactive inorganic vapor deposition growth may cast light on the fabrication of oxide, oxyhalide, and oxysulfide films, as well as other oxynitride films.

4. Materials and Methods

4.1. Preparation of $SrTaO_2N$, $BaTaO_2N$, and $CaTaO_2N$ Films. Ta foils (10 mm × 15 mm × 0.2 mm, ZhongNuo Advanced Material Co., 99.95%) were cleaned in ethanol and acetone. $SrTaO_2N$ films were prepared on a Ta foil substrate by a reactive inorganic vapor deposition method under a flow of NH_3. Briefly, 0.2 g of $SrCl_2/SrCO_3$ eutectic salt, which consisted of 26 mol% $SrCO_3$ (Sinopharm Chemical Reagent Co., 99.5%)

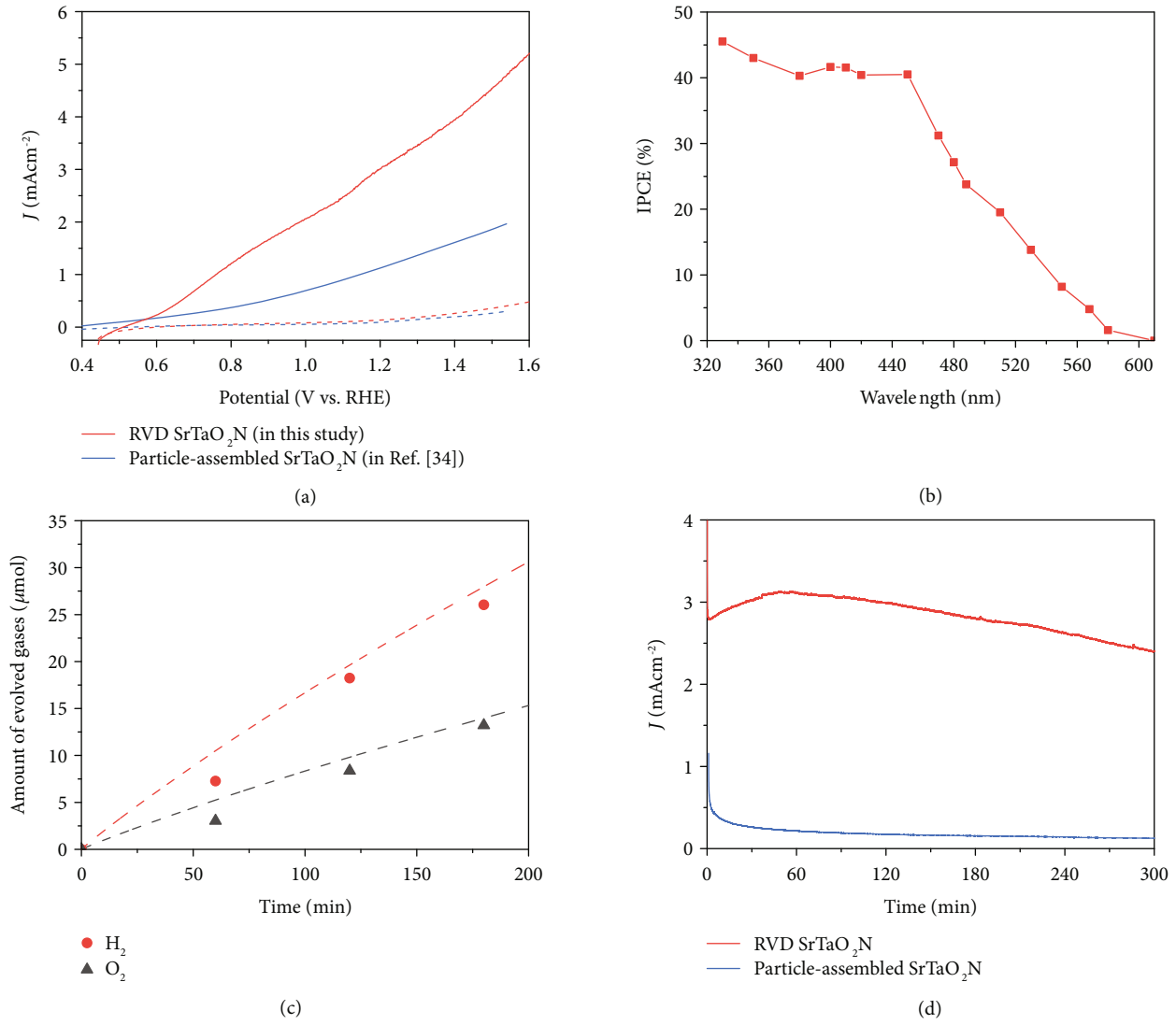

FIGURE 5: PEC performance and faradaic efficiency. (a) Photocurrents of the directly prepared $SrTaO_2N$ film and particle-assembled $SrTaO_2N$ photoanodes [34] in 1 M NaOH (pH = 13.6) electrolyte under AM 1.5G (100 mW cm^{-2}) simulated sunlight and a scan rate of 30 mV s^{-1}. (b) Wavelength dependence on the incident photon-to-current conversion efficiency (IPCE) of the $SrTaO_2N$ film photoanode with the Co/CoOOH catalyst layer measured at 1.23 V vs. RHE in 1 M NaOH (pH = 13.6) aqueous solution. (c) Gas chromatography for O_2 and H_2 generated from the $SrTaO_2N$ film photoanode modified with the Co/CoOOH layer and Pt counter electrode during PEC water splitting at an applied potential of 1.23 V vs. RHE for 180 min. (d) *I-t* curve for the $SrTaO_2N$ film photoanode and particle-assembled $SrTaO_2N$ photoanodes during PEC water splitting at 1.23 V vs. RHE (for 240 min) under AM 1.5G (100 mW cm^{-2}) illumination.

and 74 mol% $SrCl_2{\cdot}6H_2O$ (Sinopharm Chemical Reagent Co., 99.5%), was placed in an alumina combustion boat. Ta foils were put on the top of the alumina combustion boat in a sealed quartz tube furnace. The Ta foils were then annealed at 950°C for 2 hours under a flow of ammonia gas (flow rate: 250 sccm) at a rate of 10°C/min. The samples were then cooled to room temperature with the flow of ammonia gas. After the ammonolysis process, the obtained $SrTaO_2N$ photoanodes were washed with sufficient deionized water and dried overnight in air before testing. $BaTaO_2N$ and $CaTaO_2N$ films were synthesized by using the corresponding flux agents of $BaCl_2$ (74%)/$BaCO_3$ (26%) and $CaCl_2$ (74%)/$CaCO_3$ (26%), respectively. $SrNbO_2N$ and $BaNbO_2N$ films were synthesized at the same condition by using Nb foil as a precursor and corresponding flux of $SrCl_2$ (74%)/$SrCO_3$ (26%) and $BaCl_2$ (74%)/$BaCO_3$ (26%), respectively.

4.2. Photoassisted Electrodeposition of Co/CoOOH Catalysts. A two-step electrodeposition method [36] was introduced to deposit a Co/CoOOH catalyst layer from a solution of 10 mM $CoSO_4$ and 40 mM potassium acetate. First, 4 mC cm^{-2} of cobalt was electrodeposited at -0.8 V vs. SCE. Then, the 4 mC cm^{-2} of the CoOOH layer was electrodeposited in chronopotentiometry mode at 0.05 mA for 80 s under illumination of a xenon lamp (Ushio, Optical Module X500).

4.3. Structural Characterization. The crystal structures of all the samples were measured by X-ray diffraction (XRD,

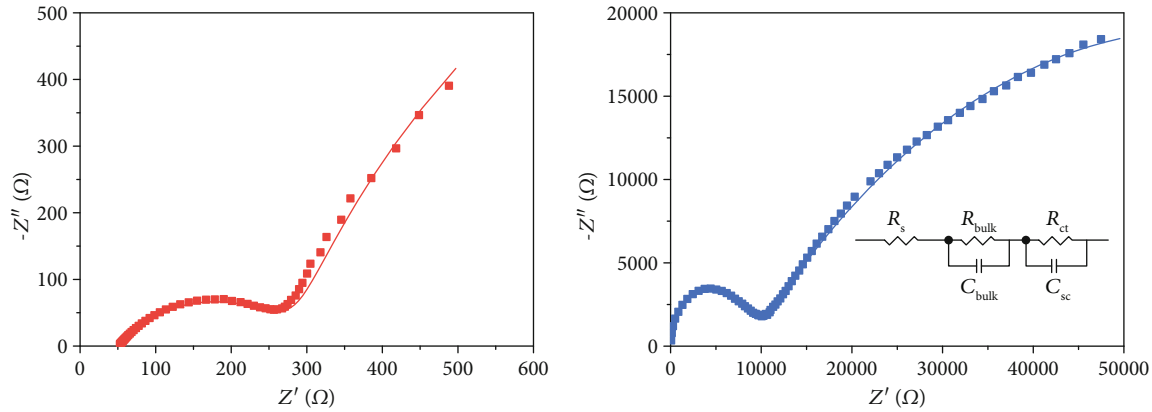

FIGURE 6: Electrochemical impedance spectroscopy measurements. Nyquist plots of the $SrTaO_2N$ film photoanode (a) and particle-assembled $SrTaO_2N$ photoanode (b) recorded at 0.6 V vs. RHE; the inset shows the equivalent circuit model.

Rigaku Ultima III) with Cu Kα radiation ($\lambda = 1.54056$ Å) at 40 kV and 40 mA. The optical absorption spectra of the $SrTaO_2N$ photoanodes were measured with a UV-visible (UV-vis) spectrophotometer (Shimadzu, UV-vis 2550). The optical band edge of the samples was determined by Tauc plots. The morphology of the films was observed by field-emission scanning electron microscopy (FE-SEM, Nova NanoSEM 230, FEI). TEM and HRTEM analysis was performed on a high-resolution transmission electron microscope (JEM-200CX). TG-DTA coupling mass spectroscopy was carried out on TG-MS equipment (NETZSCH, STA 449 F3-QMS 403 C Aëolos, Germany) in the flow of mixed N_2/NH_3 (4 mol%).

4.4. PEC Characterization. The PEC activity of $SrTaO_2N$ photoanodes was measured in a three-electrode configuration cell with a potentiostat (CHI633C) using 1 M NaOH (pH = 13.6) as the electrolyte, the $SrTaO_2N$ photoanodes as a working electrode, Hg/Hg_2Cl_2 in saturated KCl as the reference electrode, and Pt foil as the counter electrode. The CoOOH catalyst was activated by scanning from the open-circuit potential to 2.5 V vs. RHE in 1 M NaOH before the PEC measurements [36]. Measured potentials vs. Hg/Hg_2Cl_2 reference electrode were calibrated to reversible hydrogen electrode (RHE). AM 1.5G simulated sunlight (100 mW cm^{-2}) was obtained from a Newport Sol3A Class AAA simulator, and the light intensity was calibrated at 100 mW cm^{-2} by a standard reference Newport 91150 silicon cell before testing. The backsides of the $SrTaO_2N$ films were covered with AB glue and dried overnight before the PEC testing. The wavelength dependence of the incident photon-to-current efficiency (IPCE) was measured under monochromatic light irradiation from a xenon lamp (Ushio, Optical Module X500) equipped with 330-600 nm band pass filters. The light intensity of each wavelength was obtained with a photometer (Newport, 840-C). The applied bias photon-to-current efficiency (ABPE) was calculated from the *J-V* curve of the photoanode under AM 1.5G simulated sunlight.

4.5. Electrochemical Impedance Spectroscopy Measurements. Electrochemical impedance spectroscopy measurements were performed using an electrochemical analyzer (Solartron 1260+1287) with a frequency range of 0.1 Hz-100 kHz. All the measurements were obtained at room temperature at an applied potential of 0.6 V vs. RHE under dark conditions. The EIS spectral data were fitted to the electrical analogue using ZView software.

Conflicts of Interest

The authors declare no competing financial interests.

Authors' Contributions

Z. Li and T. Fang conceived and designed the research. T. Fang fabricated the samples and performed the XRD, UV-vis absorbance spectroscopy, Mott-Schottky plots, PEC experiments, SEM observation, EDS mapping, and TEM image and TG-MS analysis. H. Huang and Y. Hu helped with the photoelectrode fabrication and carried out electrochemical impedance spectroscopy. J. Feng and Q. Qian helped with the measurement of faradic efficiency. S. Yan, Z. Yu, and Z. Zou discussed the results and helped with the revision of the paper. T. Fang and Z. Li analyzed the data and wrote the paper.

Acknowledgments

This work is supported by the National Key Research and Development Program of China (No. 2018YFA0209303), the National Natural Science Foundation of China (Nos. U1663228 and 21473090), and a Project Funded by the Priority Academic Program Development of Jiangsu Higher Education Institutions. Z. L. thanks Prof. Xizhang Wang (School of Chemistry and Chemical Engineering, Nanjing University) for the nice discussion.

Supplementary Materials

Figure S1: phase diagram of the system $SrCl_2$-$SrCO_3$. Figure S2: top-down SEM image of the $SrTaO_2N$ film. Figure S3: SAED pattern of the $SrTaO_2N$ film. Figure S4: *I-V* characteristics of the $SrTaO_2N$ film. Figure S5: XRD patterns of control experiments. Figure S6: XPS spectra from 220 eV to 180 eV. Figure S7: XPS spectra of C1s. Figure S8: TEM and HRTEM images of the peeled SrTaO2N particles. Figure S9: photocurrents of the $SrTaO_2N$ film prepared with different compositions of the $SrCl_2/SrCO_3$ flux reagent. Figure S10: SEM image of the CoOOH catalyst layer. Figure S11: UV-vis diffuse reflectance spectra and Tauc plot of the $SrTaO_2N$ film. Figure S12: derived photocurrent of the $SrTaO_2N$ film. Figure S13: ABPE of $SrTaO_2N$ film photoanode and particle-assembled $SrTaO_2N$ photoanode. Figure S14: Mott-Schottky plots of the $SrTaO_2N$ film. Figure S15: XRD patterns of $CaTaO_2N$ and $BaTaO_2N$ films. Figure S16: SEM images of $CaTaO_2N$ and $BaTaO_2N$ films. Figure S17: HRTEM images of $CaTaO_2N$ and $BaTaO_2N$ films. Figure S18: XRD patterns and SEM images of $SrNbO_2N$ and $BaNbO_2N$ films. Figure S19: *J-V* curves of the $CaTaO_2N$ film, $BaTaO_2N$ film, $SrNbO_2N$ film, and $BaNbO_2N$ film. Table S1: the fitted values of R_{bulk}. Table S2: Water oxidation onset potentials and solar photocurrents of $SrTaO_2N$ photoanodes. *(Supplementary Materials)*

References

[1] M. Yang, J. Oró-Solé, J. A. Rodgers, A. B. Jorge, A. Fuertes, and J. P. Attfield, "Anion order in perovskite oxynitrides," *Nature Chemistry*, vol. 3, no. 1, pp. 47–52, 2011.

[2] M. Jansen and H. P. Letschert, "Inorganic yellow-red pigments without toxic metals," *Nature*, vol. 404, no. 6781, pp. 980–982, 2000.

[3] X. Gouin, R. Marchand, Y. Laurent, and F. Gervais, "Infrared dielectric response in $BaTaO_2N$," *Solid State Communications*, vol. 93, no. 10, pp. 857–859, 1995.

[4] Y.-I. Kim, P. M. Woodward, K. Z. Baba-Kishi, and C. W. Tai, "Characterization of the structural, optical, and dielectric properties of oxynitride perovskites AMO_2N (A = Ba, Sr, Ca; M = Ta, Nb)," *Chemistry of Materials*, vol. 16, no. 7, pp. 1267–1276, 2004.

[5] T. Yajima, F. Takeiri, K. Aidzu et al., "A labile hydride strategy for the synthesis of heavily nitridized $BaTiO_3$," *Nature Chemistry*, vol. 7, no. 12, pp. 1017–1023, 2015.

[6] A. B. Jorge, J. Oró-Solé, A. M. Bea et al., "Large coupled magnetoresponses in $EuNbO_2N$," *Journal of the American Chemical Society*, vol. 130, no. 38, pp. 12572-12573, 2008.

[7] A. Kasahara, K. Nukumizu, G. Hitoki et al., "Photoreactions on $LaTiO_2N$ under visible light irradiation," *The Journal of Physical Chemistry A*, vol. 106, no. 29, pp. 6750–6753, 2002.

[8] B. Siritanaratkul, K. Maeda, T. Hisatomi, and K. Domen, "Synthesis and photocatalytic activity of perovskite niobium oxynitrides with wide visible-light absorption bands," *ChemSusChem*, vol. 4, no. 1, pp. 74–78, 2011.

[9] I. E. Castelli, D. D. Landis, K. S. Thygesen et al., "New cubic perovskites for one- and two-photon water splitting using the computational materials repository," *Energy & Environmental Science*, vol. 5, no. 10, pp. 9034–9043, 2012.

[10] M. Grätzel, "Photoelectrochemical cells," *Nature*, vol. 414, no. 6861, pp. 338–344, 2001.

[11] S. Hu, M. R. Shaner, J. A. Beardslee, M. Lichterman, B. S. Brunschwig, and N. S. Lewis, "Amorphous TiO_2 coatings stabilize Si, GaAs, and GaP photoanodes for efficient water oxidation," *Science*, vol. 344, no. 6187, pp. 1005–1009, 2014.

[12] O. Khaselev and J. A. Turner, "A monolithic photovoltaic-photoelectrochemical device for hydrogen production via water splitting," *Science*, vol. 280, no. 5362, pp. 425–427, 1998.

[13] M. Zhou, X. W. (David) Lou, and Y. Xie, "Two-dimensional nanosheets for photoelectrochemical water splitting: possibilities and opportunities," *Nano Today*, vol. 8, no. 6, pp. 598–618, 2013.

[14] Y. Cong, H. S. Park, S. Wang et al., "Synthesis of Ta3N5Nanotube arrays modified with electrocatalysts for photoelectrochemical water oxidation," *The Journal of Physical Chemistry C*, vol. 116, no. 27, pp. 14541–14550, 2012.

[15] J.-W. Jang, C. Du, Y. Ye et al., "Enabling unassisted solar water splitting by iron oxide and silicon," *Nature Communications*, vol. 6, no. 1, article 7447, 2015.

[16] G. Liu, J. Shi, F. Zhang et al., "A tantalum nitride photoanode modified with a hole-storage layer for highly stable solar water splitting," *Angewandte Chemie International Edition*, vol. 53, no. 28, pp. 7295–7299, 2014.

[17] M. G. Kibria, S. Zhao, F. A. Chowdhury et al., "Tuning the surface Fermi level on *p*-type gallium nitride nanowires for efficient overall water splitting," *Nature Communications*, vol. 5, no. 1, p. 3825, 2014.

[18] S. J. A. Moniz, S. A. Shevlin, D. J. Martin, Z.-X. Guo, and J. Tang, "Visible-light driven heterojunction photocatalysts for water splitting - a critical review," *Energy & Environmental Science*, vol. 8, no. 3, pp. 731–759, 2015.

[19] M. Davi, F. Schrader, T. Scholz et al., "$SrTaO_2N$ nanowire photoanode modified with a ferrihydrite hole-storage layer for photoelectrochemical water oxidation," *ACS Applied Nano Materials*, vol. 1, no. 2, pp. 869–876, 2018.

[20] J. Feng, W. Luo, T. Fang et al., "Highly photo-responsive LaTiO2N photoanodes by improvement of charge carrier transport among film particles," *Advanced Functional Materials*, vol. 24, no. 23, pp. 3535–3542, 2014.

[21] L. Zhang, Y. Song, J. Feng et al., "Photoelectrochemical water oxidation of $LaTaON_2$ under visible-light irradiation," *International Journal of Hydrogen Energy*, vol. 39, no. 15, pp. 7697–7704, 2014.

[22] H. Huang, J. Feng, H. Fu et al., "Improving solar water-splitting performance of $LaTaON_2$ by bulk defect control and interface engineering," *Applied Catalysis B: Environmental*, vol. 226, no. 15, pp. 111–116, 2018.

[23] M. Higashi, K. Domen, and R. Abe, "Fabrication of an efficient $BaTaO_2N$ photoanode harvesting a wide range of visible light for water splitting," *Journal of the American Chemical Society*, vol. 135, no. 28, pp. 10238–10241, 2013.

[24] C. Zhen, R. Chen, L. Wang, G. Liu, and H.-M. Cheng, "Tantalum (oxy)nitride based photoanodes for solar-driven water oxidation," *Journal of Materials Chemistry A*, vol. 4, no. 8, pp. 2783–2800, 2016.

[25] Y.-I. Kim, "Effects of KCl flux on the morphology, anion composition, and chromaticity of perovskite oxynitrides, $CaTaO_2N$, $SrTaO_2N$, and $LaTaON_2$," *Ceramics International*, vol. 40, no. 4, pp. 5275–5281, 2014.

[26] A. Rachel, S. G. Ebbinghaus, M. Güngerich et al., "Tantalum and niobium perovskite oxynitrides: synthesis and analysis of the thermal behaviour," *Thermochimica Acta*, vol. 438, no. 1–2, pp. 134–143, 2005.

[27] I. D. Fawcett, K. V. Ramanujachary, and M. Greenblatt, "Synthesis, structure and properties of the oxynitrides $SrWO_2N$ and $SrMoO_{2.5}N_{0.5}$," *Materials Research Bulletin*, vol. 32, no. 11, pp. 1565–1570, 1997.

[28] E. Günther, R. Hagenmayer, and M. Jansen, "Strukturuntersuchungen an den oxidnitriden $SrTaO_2N$, $CaTaO_2N$ und $LaTaON_2$ mittels Neutronen- und Röntgenbeugung," *Zeitschrift für Anorganische und Allgemeine Chemie*, vol. 626, no. 7, pp. 1519–1525, 2000.

[29] S. J. Clarke, B. P. Guinot, C. W. Michie, M. J. C. Calmont, and M. J. Rosseinsky, "Oxynitride perovskites: synthesis and structures of $LaZrO_2N$, $NdTiO_2N$, and $LaTiO_2N$ and comparison with oxide perovskites," *Chemistry of Materials*, vol. 14, no. 1, pp. 288–294, 2002.

[30] D. Eisenberg, H. S. Ahn, and A. J. Bard, "Enhanced photoelectrochemical water oxidation on bismuth vanadate by electrodeposition of amorphous titanium dioxide," *Journal of the American Chemical Society*, vol. 136, no. 40, pp. 14011–14014, 2014.

[31] Z. Li, J. Feng, S. Yan, and Z. Zou, "Solar fuel production: strategies and new opportunities with nanostructures," *Nano Today*, vol. 10, no. 4, pp. 468–486, 2015.

[32] T. Fang, H. Huang, J. Feng et al., "Exploring facile strategies for high-oxidation-state metal nitride synthesis: carbonate-assisted one-step synthesis of Ta_3N_5 films for solar water splitting," *Science Bulletin*, vol. 63, no. 21, pp. 1404–1410, 2018.

[33] A. M. Martre and P. Pouillen, "Contribution à la détermination du diagramme binaire $SrCl_2$-$SrCO_3$," *Comptes Rendus de l'Académie des Sciences*, vol. 263, pp. 1477–1480, 1966.

[34] Y. Zhong, Z. Li, X. Zhao et al., "Enhanced water-splitting performance of perovskite SrTaO2N photoanode film through ameliorating interparticle charge transport," *Advanced Functional Materials*, vol. 26, no. 39, pp. 7156–7163, 2016.

[35] B. A. Pinaud, P. C. K. Vesborg, and T. F. Jaramillo, "Effect of film morphology and thickness on charge transport in Ta_3N_5/Ta photoanodes for solar water splitting," *The Journal of Physical Chemistry C*, vol. 116, no. 30, pp. 15918–15924, 2012.

[36] J. C. Hill, A. T. Landers, and J. A. Switzer, "An electrodeposited inhomogeneous metal–insulator–semiconductor junction for efficient photoelectrochemical water oxidation," *Nature Materials*, vol. 14, no. 11, pp. 1150–1155, 2015.

[37] D. K. Zhong, M. Cornuz, K. Sivula, M. Grätzel, and D. R. Gamelin, "Photo-assisted electrodeposition of cobalt–phosphate (Co–Pi) catalyst on hematite photoanodes for solar water oxidation," *Energy & Environmental Science*, vol. 4, no. 5, pp. 1759–1764, 2011.

[38] S. Balaz, S. H. Porter, P. M. Woodward, and L. J. Brillson, "Electronic structure of tantalum oxynitride perovskite photocatalysts," *Chemistry of Materials*, vol. 25, no. 16, pp. 3337–3343, 2013.